# Comparison of the macroscopic behavior of granular materials modeled by different constitutive equations on the microscale

C. Wellmann[1], C. Lillie and P. Wriggers

*Institute of Mechanics and Computational Mechanics, Leibniz-University of Hannover*
*Appelstr. 9a, D-30167 Hannover, Germany*

**Abstract**

In this paper a three-dimensional Discrete Element Method (DEM) is used to model cohesionless granular materials. Two different microscopic constitutive equations are used to resolve the contacts between single particles in the DEM: First, a simple penalty type contact law and second, a more sophisticated HERTZIAN type contact law. Numerical tests in form of DEM simulations of a cuboid particle sample under compression and shearing are performed using both microscopic constitutive equations. The microscopic results of the DEM in terms of inter-particle contact forces and particle trajectories are transferred to macroscopic results in terms of stresses and strains by a homogenization approach. The macroscopic results are presented and compared for the different microscopic constitutive equations.

*Keywords:* DEM, homogenization, HERTZIAN contact, granular material

## 1 Introduction

A common approach for the numerical modeling of granular materials is to consider the actually discontinuous material as continuum on the macroscale. A macroscopic constitutive equation is then required to model the response of the material to a given set of boundary conditions. On the one hand the benefit of this approach is that large scale problems become feasible through application of e.g. the finite-element method. On the other hand a major drawback is that a macroscopic constitutive equation which is able to predict the various complicated effects exerted by granular materials is hardly found. Attempts to do so often result in macroscopic equations including a huge number of parameters some of which having an obscure physical meaning. Therefore, an interesting alternative for the numerical modeling of granular materials is the Discrete Element Method (DEM) which was introduced by Cundall and Strack [6]. Within a DEM the individual grains are modeled as rigid bodies which interact through contact forces. This has the advantage that the complicated macroscopic behavior arises as an emergent property of a huge assembly of particles. In this way the complex macroscopic constitutive

[1]Corresponding author. Tel.: +49 511-762.2285; fax: +49 511-762.5496; E-mail: wellmann@ibnm.uni-hannover.de

equation is replaced by a rather simple constitutive equation on the particle level based on a relative small number of parameters. The drawback of this approach is its high computational cost, but with increasing computational power and memory large scale problems are expected to become feasible in the future, see [4] for a detailed discussion.

In this paper two different microscopic constitutive equations are used within a three-dimensional DEM that models cohesionless granular materials: First, a simple penalty contact formulation, which has the drawback that the penalty parameters lack of a real physical meaning. Second, a more sophisticated HERTZIAN type contact law, in which the penalty parameters are replaced by the elastic constants of the particles. To compare these contact laws in terms of the macroscopic behavior that arise from them, DEM simulations of a compression and a shear test of a cuboid particle sample are performed. The microscopic results in terms of inter-particle contact forces and particle trajectories from the DEM are transferred to a macroscopic description in terms of stresses and strains via a homogenization procedure. Therefore a number of representative volume elements (RVEs) are defined inside the particle sample which are then used as averaging volume for the macroscopic quantities. The results are evaluated as ensemble averages over the RVEs and compared for the different microscopic constitutive equations.

The paper is organized as follows: Section 2 briefly describes the important features of the DEM used to model the granular materials whereat the microscopic constitutive equations are discussed in detail in section 3. The model and test setup for the numerical compression and shear tests are outlined in section 4. Section 5 gives a short description of the homogenization approach used for the analysis of the DEM results. Finally, the results of the numerical tests are presented in section 6 which is followed by a conclusion.

## 2 Discrete Element Method

The Discrete Element Method (DEM) is a numerical scheme to model the mechanical behavior of a large number of particles. Commonly, every particle is considered as a rigid body with the translational and rotational degrees of freedom assigned to their centers of mass. An explicit time integration scheme is applied to the particles equations of motion to keep track of the particle positions and velocities. While moving, some of the particles will contact. Hence, a proper contact formulation is required to handle the contacts by application of repulsive contact forces, which prevent the particles from moving through each over. In this paper two different contact formulations are compared, which will be described in section 3. In the rest of this section the other features of the DEM used here will be discussed briefly.

DEMs generally differ in the dimensionality of the considered system, the shape of the particles

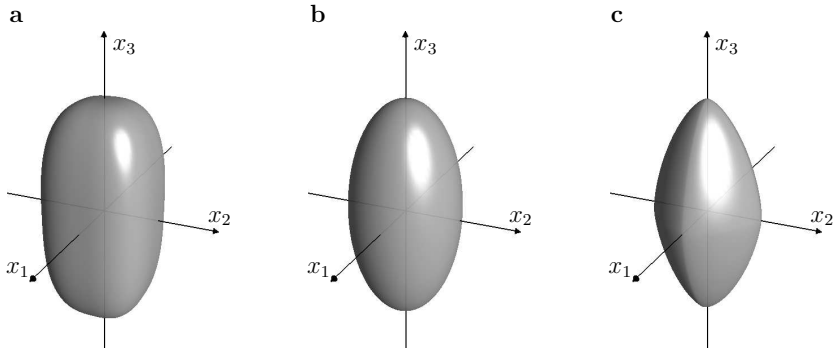


Fig. 1. Superellipsoids with $r_1 = r_2 = r_3/2$ and $\epsilon_i = 0.7$ (a), $\epsilon_i = 1$ (b) and $\epsilon_i = 1.3$ (c).

and the contact formulation. Most of the DEMs used today work with two-dimensional systems because the computational effort required even when working with a moderate number of particles can be reduced significantly by working in two instead of three dimensions. This is mainly due to the fact that the determination of particle contacts and the handling of particle rotations is much cheaper in two dimensions. Anyway, the authors believe that the situation of a three-dimensional packing of particles and the corresponding possibilities of relative particle motions might not be represented well by a two-dimensional model. Hence, a three-dimensional model is used here.

Regarding the particle type it can be said that the vast majority of todays three-dimensional DEM codes use spherical particles because of the minimum costs for contact detection. However, regarding soil mechanics, it is known that the geometry of real grains is not modeled well by spheres, compare e.g. [14]. Through a comparison of spherical and ellipsoidal particles Lin and Ng [10] showed that the main problem with spherical particles is their small resistance against rolling. To overcome this problem several other particle shapes have been proposed, e.g. polyhedral particles [5], particles that are build of clusters of spheres [15], oval particles that are build of arcs [16] and particles based on potential functions [18]. Here superellipsoid particles as proposed in [3] are used, which have a smooth surface and therefore uniquely defined outward normals, a feature which is favorable for calculation of contact forces. Further, a superellipsoid allows for arbitrary aspect ratios in three dimensions yielding the desired interlocking phenomena described in [10]. It is defined by five parameters through the geometric potential function

$$F(\boldsymbol{x}) = \left( \left| \frac{x_1}{r_1} \right|^{\frac{2}{\epsilon_1}} + \left| \frac{x_2}{r_2} \right|^{\frac{2}{\epsilon_1}} \right)^{\frac{\epsilon_1}{\epsilon_2}} + \left| \frac{x_3}{r_3} \right|^{\frac{2}{\epsilon_2}} \quad \text{with} \quad \epsilon_1, \epsilon_2 \in (0, 2) \; . \tag{1}$$

Every point $\boldsymbol{x}$ inside the superellipsoid obeys $F(\boldsymbol{x}) < 1$ and every surface point $\boldsymbol{x}$ obeys $F(\boldsymbol{x}) = 1$. The dimensions of the superellipsoid are specified by the radius parameters $r_i$ while the exponents $\epsilon_i$ control its squareness, compare Fig. 1.

The equations of motion of a single particle $\mathcal{P}^i$ with its mass $m^i$, center of mass $\boldsymbol{x}^i$, inertia tensor

$\boldsymbol{J}^i$ and rotational velocity $\boldsymbol{\omega}^i$ read

$$m^i \ddot{\boldsymbol{x}}^i = \sum_{j=1}^{N_c^i} \boldsymbol{f}^{ij} + \boldsymbol{g}^i + \boldsymbol{f}_d^i \,, \tag{2}$$

$$\boldsymbol{J}^i \cdot \dot{\boldsymbol{\omega}}^i + \boldsymbol{\omega}^i \times \boldsymbol{J}^i \cdot \boldsymbol{\omega}^i = \sum_{j=1}^{N_c^i} \boldsymbol{m}^{ij} + \boldsymbol{m}_d^i \,. \tag{3}$$

Herein $N_c^i$ is the number of contacts of $\mathcal{P}^i$, $\boldsymbol{f}^{ij}$ is the contact force between $\mathcal{P}^i$ and $\mathcal{P}^j$ and $\boldsymbol{m}^{ij}$ is the resulting moment of $\boldsymbol{f}^{ij}$ with respect to the center of mass. $\boldsymbol{g}^i$ is the gravitation force and $\boldsymbol{f}_d^i$ is a viscous damping force that is introduced in order to reach an equilibrium state in minimum time. The same holds true for the viscous damping moment $\boldsymbol{m}_d^i$. For the solution of these equations two different time integration schemes are applied: The third order VERLET-LEAPFROG method for the translational part and the fourth order RUNGE-KUTTA method for the rotational part. These integrators show good properties regarding the conservation of energy and momentum during the simulation.

# 3 Contact Formulation

In DEMs using explicit time integration schemes to resolve the particle trajectories small interpenetrations of adjacent particles have to be admitted in order to be able to generate inter-particle contact forces. For this purpose different contact formulations have been proposed whose applicability often depends on the kind of particle shape that is used. In this paper two different contact formulations are compared. First, a simple penalty type contact formulation and second, a more sophisticated HERTZIAN type contact formulation. Both of them require a description of the contact geometry of two penetrating particles. For the penalty contact formulation this description consists of the definition of contact points and a contact normal. For the HERTZIAN contact formulation the principal curvatures and their directions at the contact points are needed in addition.

For two penetrating particles $\mathcal{P}^i$ and $\mathcal{P}^j$ the contact points are defined as those points on the particle surfaces who have minimum distance and whose outward pointing unit normals are antiparallel, see Fig. 2. If the interpenetration is small compared to the particle size and the minimum radius of curvature these conditions yield unique contact points. The penalty type contact formulation penalizes the interpenetration of $\mathcal{P}^i$ and $\mathcal{P}^j$ by application of a repulsive contact force between them. We denote the force acting on $\mathcal{P}^i$ with $\boldsymbol{f}^i =: \boldsymbol{f}$ and the force acting on $\mathcal{P}^j$ with $\boldsymbol{f}^j = -\boldsymbol{f}$. For calculation $\boldsymbol{f}$ is split into a normal and a tangential part

$$\boldsymbol{f} = \boldsymbol{f}^N + \boldsymbol{f}^T = -f^N \boldsymbol{n}^i + \boldsymbol{f}^T. \tag{4}$$

The normal part consists of an elastic term which is proportional to the interpenetration distance

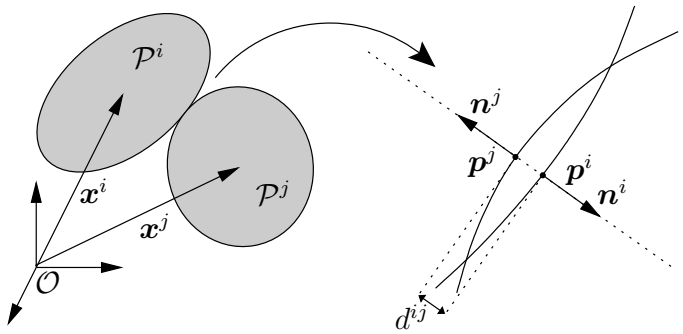


Fig. 2. Two penetrating particles with contact points, normal vectors and the interpenetration distance.

and a viscous term which is introduced to reduce the particle oscillations

$$f^N = c^N \, d^{ij} + D \left( \boldsymbol{v} \cdot \boldsymbol{n}^i \right). \tag{5}$$

Herein $c^N$ is the normal penalty parameter and $\boldsymbol{v} = \dot{\boldsymbol{p}}^i - \dot{\boldsymbol{p}}^j$ is the relative velocity of the contact points. Critical damping is achieved by choosing the damping parameter as

$$D = 2\sqrt{c^N \frac{m^i \, m^j}{m^i + m^j}}. \tag{6}$$

The tangential part of the contact force has to be computed incrementally and is bounded by the normal part through Coulomb's friction law. Hence, the tangential force in the current time-step $\boldsymbol{f}_n^T$ is derived from the tangential force in the last time-step $\boldsymbol{f}_{n-1}^T$ in a two step scheme. First, a trial value is computed as

$$\boldsymbol{f}_{\mathrm{tr}}^T = \boldsymbol{f}_{n-1}^T - c^T \, \Delta t \, \boldsymbol{v}^T. \tag{7}$$

Herein $c^T$ is the tangential penalty parameter, $\Delta t$ is the time-step length and $\boldsymbol{v}^T$ is the tangential part of the relative velocity. Hence, $\Delta t \, \boldsymbol{v}^T$ is the approximated tangential displacement of the contact points in the current time-step. The tangential force in the actual time-step results from Coulomb's criterion

$$\boldsymbol{f}_n^T = \begin{cases} \boldsymbol{f}_{\mathrm{tr}}^T, & \text{if} \quad \| \boldsymbol{f}_{\mathrm{tr}}^T \| \leq \mu \, |f^N| \\ \mu \, |f^N| \, \frac{\boldsymbol{f}_{\mathrm{tr}}^T}{\| \boldsymbol{f}_{\mathrm{tr}}^T \|}, & \text{else.} \end{cases} \tag{8}$$

Next, the Hertzian contact theory [8] will be applied to resolve the contacts with respect to the explicit time integration scheme used in the DEM. Herein Mindlin's results [11] will be used for the tangential part of the contact force. A detailed description of the Hertzian contact theory can be found in many textbooks, see e.g. [9] or [7]. For convenience a summary of its main assumptions and results will be given here. The first important assumption made by Hertz is that the contacting bodies are homogeneous, isotropic and elastic solids. Further, it is assumed that their surfaces are smooth and non-conforming so that contact forms at a single point which evolves to an area of contact when the contacting particles are pressed together. Hertz

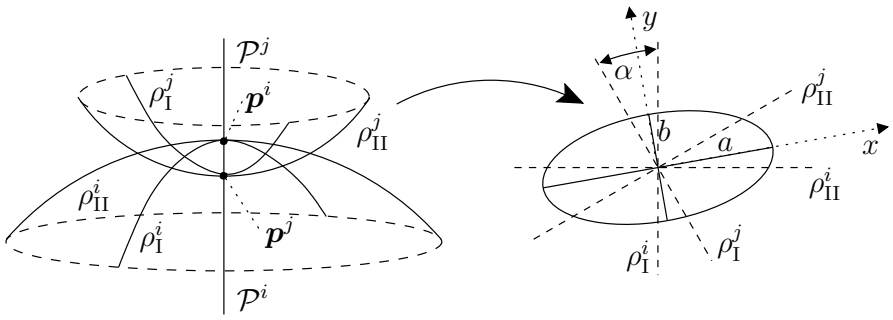


Fig. 3. Paraboloids approximating the particle surfaces at the contact points.

discovered that this contact area is of elliptical shape. Regarding each of the contact partners as an elastic half space loaded over an elliptical region HERTZ was able to derive contact pressures by applying the theory of linear elasticity. For this approach to be reasonable the dimension of the contact area has to be small compared to

- the size of the bodies, so that the concentrated stresses in the contact area are not affected from outside the contact area and
- to the radii of curvature of the surfaces, so that the surfaces approximate an elastic half space and the strains in the contact region are small enough for the theory of linear elasticity to be applicable.

Regarding the superellipsoid particles used in the DEM as homogeneous, isotropic and elastic the above conditions are fulfilled since superellipsoids have a smooth convex shape and the interpenetration of adjacent particles is much smaller than the particle dimensions. Note, that the interpenetration distance will now be considered as the normal approach of two distant points inside the contacting particles and that the interpenetration is considered as an elastic deformation of the particles at the contact. For the derivation of a contact force the description of the contact geometry used for the penalty contact formulation has to be extended. HERTZ approximates the particle surfaces in the contact region by paraboloids defined by the principal curvatures $\rho_{\mathrm{I}}$ and $\rho_{\mathrm{II}}$ of the surfaces at the contact points and their corresponding perpendicular directions, see Fig. 3. From this description the shape of the contact ellipse which is defined by the ratio of its semi-axes $\kappa = a/b$ (with $b \leq a$) can be derived. Therefore, the so called relative curvatures $A$ and $B$ (with $A \leq B$) are introduced

$$(A+B) = \frac{1}{2}\left(\rho^i_{\mathrm{I}} + \rho^i_{\mathrm{II}} + \rho^j_{\mathrm{I}} + \rho^j_{\mathrm{II}}\right), \tag{9}$$

$$|A-B| = \frac{1}{2}\sqrt{(\rho^i_{\mathrm{I}} - \rho^i_{\mathrm{II}})^2 + (\rho^j_{\mathrm{I}} - \rho^j_{\mathrm{II}})^2 + 2\,(\rho^i_{\mathrm{I}} - \rho^i_{\mathrm{II}})\,(\rho^j_{\mathrm{I}} - \rho^j_{\mathrm{II}})\cos 2\,\alpha}\,. \tag{10}$$

The first main result of HERTZ is that $\kappa$ depends on the ratio of the relative curvatures $B/A$

solely. The relation is given implicitly through

$$\frac{B}{A} = \frac{(1/\kappa)^2\ E(e) - K(e)}{K(e) - E(e)} \quad \text{with} \quad e = \sqrt{1 - \frac{1}{\kappa^2}}\,. \tag{11}$$

Herein $e$ is called the eccentricity of the contact ellipse and $K(e)$ and $E(e)$ denote the complete elliptic integrals of the first and second kind, respectively. Since it is not possible to solve equation (11) for $\kappa$ explicitly an approximate analytical scheme presented in [2] is used which yields a maximum relative error for $\kappa$ of $5.86 \times 10^{-6}$ for a range of $1 \leq B/A \leq 10^{10}$. Introducing $E^*$ through

$$\frac{1}{E^*} = \frac{1 - \left(\nu^i\right)^2}{E^i} + \frac{1 - \left(\nu^j\right)^2}{E^j}\,, \tag{12}$$

where $\nu$ denotes Poisson's ratio and $E$ denotes the elastic modulus of a particle the normal part of the contact force is given by

$$f^N = \underbrace{\frac{2}{3}\,\pi\,\kappa\,\sqrt{\frac{E(\kappa)}{K(\kappa)^3\ (A+B)}}}_{\gamma}\ E^*\ \left(d^{ij}\right)^{(3/2)} + D\left(\boldsymbol{v}\cdot\boldsymbol{n}^i\right). \tag{13}$$

Herein $\gamma$ is a function of the principal curvatures and their directions solely and therefore will be constant if the contact points and the relative orientation of the particles are constant. The elliptic integrals are approached using expressions that can be found in [1] and [2]. The damping parameter is chosen according to the current normal contact stiffness $k^N$

$$k^N = \frac{\partial f^N}{\partial d^{ij}} = (3/2)\,\gamma\,E^*\,\sqrt{d^{ij}}\,, \tag{14}$$

$$D = 2\sqrt{k^N \frac{m^i\,m^j}{m^i + m^j}}\,. \tag{15}$$

For the derivation of the tangential contact force the results of Mindlin [11] are used who considered the same system as Hertz when the contacting bodies are not only pressed together in the direction of the contact normal but also sheared by application of a tangential force. Additionally to the assumptions and simplifications that were made by Hertz, Mindlin assumed that no slip occurs between the bodies in contact. He was then able to show that the shape and size of the area of contact is not influenced by the tangential load and derived elastic compliances for the relative movement of the bodies in the directions of the semi-axes of the contact ellipse. Therefore, two functions of $e$ are introduced

$$B(e) = \frac{E(e) - \left(1 - e^2\right)\ K(e)}{e^2}\,, \tag{16}$$

$$D(e) = \frac{K(e) - E(e)}{e^2}\,. \tag{17}$$

The first semi-axis of the contact ellipse can now be calculated as

$$a = \sqrt{\frac{d^{ij}\ D(e)}{A\,K(e)}}\,. \tag{18}$$

Introducing the material constants

$$\lambda_1 = \frac{1+\nu^i}{E^i} + \frac{1+\nu^j}{E^j}\,, \tag{19}$$

$$\lambda_2 = \nu^i\,\frac{1+\nu^i}{E^i} + \nu^j\,\frac{1+\nu^j}{E^j}\,, \tag{20}$$

the elastic compliances can be written as

$$C_x = \frac{1}{\pi\,a}\,\left(K(e)\,\lambda_1 - B(e)\,\lambda_2\right)\,, \tag{21}$$

$$C_y = \frac{1}{\pi\,a}\,\left(K(e)\,\lambda_1 - D(e)\,\lambda_2\right)\,. \tag{22}$$

The tangential contact force is computed with the same two step scheme used for the penalty type contact formulation. For calculation of the trial value the tangential stiffness tensor $\boldsymbol{K}^T$ is introduced

$$\boldsymbol{K}^T = \frac{1}{C_x}\,\boldsymbol{e}_x \otimes \boldsymbol{e}_x + \frac{1}{C_y}\,\boldsymbol{e}_y \otimes \boldsymbol{e}_y\,, \tag{23}$$

where $\boldsymbol{e}_x$ and $\boldsymbol{e}_y$ are the unit vectors in direction of the semi-axes of the contact ellipse, see Fig. 3. Equation (7) is now replaced by

$$\boldsymbol{f}^T_{\mathrm{tr}} = \boldsymbol{f}^T_{n-1} - \boldsymbol{K}^T\,\Delta t\,\boldsymbol{v}\,. \tag{24}$$

Hence, in contrast to the penalty contact formulation and depending on the ratio of the elastic compliances the increment of the tangential contact force in general is not parallel to the increment of the relative tangential displacement. The ratio of the elastic compliances in turn depends on the shape of the contact ellipse $\kappa$ and POISSON's ratios $\nu^i$ and $\nu^j$. Generally, the elastic compliance $C_x$ in direction of the major semi-axis $a$ is greater than the elastic compliance $C_y$ in direction of the minor semi-axis $b$, where in the limit of $\kappa = 1$ it is $C_x = C_y$, of course. The dependence on POISSON's ratio is such that the compliances decrease as $\nu^i$ or $\nu^j$ increase. As can be seen from equations (20), (21) and (22) in the limit of $\nu^i = \nu^j = 0$ it is $\lambda_2 = 0$ and therefore the isotropic case $C_x = C_y$.

MINDLIN also compared the ratio of the normal compliance $C_z := 1/k^N$ (see equation (14)) and the tangential compliance $C_x$ for the case of identical elastic properties $E^i = E^j = E$ and $\nu^i = \nu^j = \nu$. Here, in the limiting case of $\nu = 0$ it is $C_z = C_x = C_y$. For the practical range of $0 \leq \nu \leq 1/2$ the tangential compliance is always greater than the normal compliance but never more than twice as great.

# 4 Test setup

The goal of this work is a comparison of the macroscopic mechanical behavior emerging from the microscopic constitutive equations described above. Therefore, the macroscopic behavior is

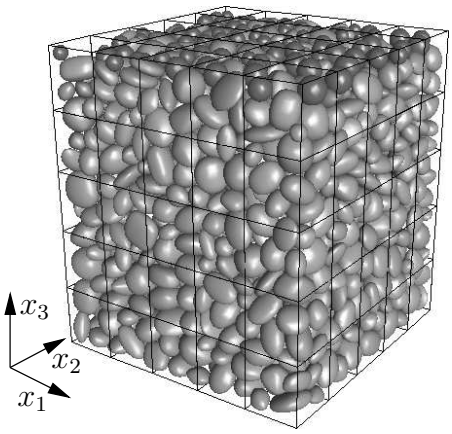


Fig. 4. Cuboid particle sample consisting of 1609 particles.

derived from the results of DEM simulations of compression and shear tests via a homogenization scheme. Since the results are compared in a qualitative way, no units will be given in the description of the model used for the DEM simulations and in the discussion of the macroscopic results in section 6.

The cuboid particle sample that is used for the numerical tests is shown in Fig. 4. This sample was created by first generating 1530 superellipsoid particles whose center of mass lie on a regular grid with a vertex distance large enough to prevent any particle interpenetrations. The parameters of each superellipsoid (compare equation (1)) were chosen randomly and equally distributed from the intervals

$$r_i \in (0.5, 1.5) \quad i = 1, 2, 3\,, \tag{25}$$

$$\epsilon_i \in (0.7, 1.3) \quad i = 1, 2\,. \tag{26}$$

Random orientations were assigned to the particles before they fell into a cuboid box with a base area of the dimensions $21.0 \times 21.0$. Under the influence of global and contact damping the particles reached a state of static equilibrium. The upper face of the box was added according to the top particle at a height of 23.6. In order to get approximately the same number of particle box contacts at the upper face like at the other faces, 79 spherical particles were fitted into the space between the upper ellipsoid particles and the upper box face. The radii off these particles, which are plotted in darker color in Fig. 4, lie also in the interval $(0.5, 1.5)$. The volume of the resulting particle package makes up 63% of the box volume which is equivalent to a void ratio of 0.59. Compression and shear tests of this particle sample were performed in form of DEM simulations whereat the particle sample was loaded by moving the faces of the surrounding box. Within these simulations the penalty parameters/elastic constants as well as the coefficient of friction were chosen identical for every contact pair/particle within the system. Furthermore the same contact formulation was used for contacts between a particle and a box face as between two particles.

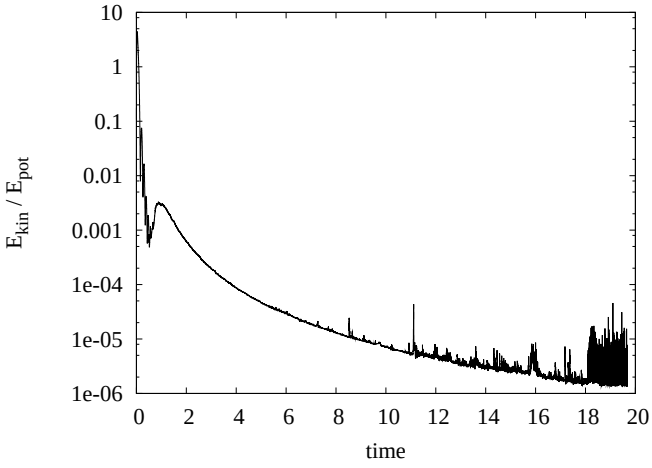


Fig. 5. Ratio of the kinetic and the potential energy vs. simulation time for a quasi static compression test .

Hence, the behavior of the system is determined by three microscopic constitutive parameters solely: The coefficient of friction $\mu$ plus the penalty parameters $c^N$ and $c^T$ for the penalty contact formulation or the elastic modulus $E$ and POISSON's ratio $\nu$ for the HERTZIAN contact formulation.

For the analysis of the results using the homogenization approach described in section 5 it is important that the imposed boundary conditions yield homogeneous macroscopic fields. In this case the different representative volume elements are expected to yield similar results what facilitates the computation of ensemble averages. The compression tests were performed by moving the upper box face downwards resulting in the homogeneous macroscopic linear strain tensor

$$\boldsymbol{\epsilon} = -\lambda\, c_{\text{end}}\, \boldsymbol{e}_3 \otimes \boldsymbol{e}_3\,. \tag{27}$$

Analogous the shear tests were performed by moving the upper box face in the $X_1$ direction, whereat the initial configuration was already compressed in the $X_3$ direction. This yields the strain tensor

$$\boldsymbol{\epsilon} = \frac{1}{2}\,\lambda\,\gamma_{\text{end}}\,(\boldsymbol{e}_1 \otimes \boldsymbol{e}_3 + \boldsymbol{e}_3 \otimes \boldsymbol{e}_1) - c_{\text{end}}\,(\boldsymbol{e}_3 \otimes \boldsymbol{e}_3)\,. \tag{28}$$

Furthermore the tests had to be performed in a quasi static way so that the resulting macroscopic values are not influenced by dynamic effects. This is accomplished by moving the box faces at a very low velocity. To check the validity of the assumption of a quasi static deformation the kinetic energy of the particles and the potential energy stored in the elastic particle-particle and particle-box contacts were recorded. Fig. 5 shows the ratio of the kinetic and the potential energy over the simulation time for a compression test. It can be seen that initially the kinetic energy exceeds the potential energy. Afterwards the ratio decreases rapidly and stays below a value of $10^{-3}$ for the rest of the simulation, so that the assumption of a quasi

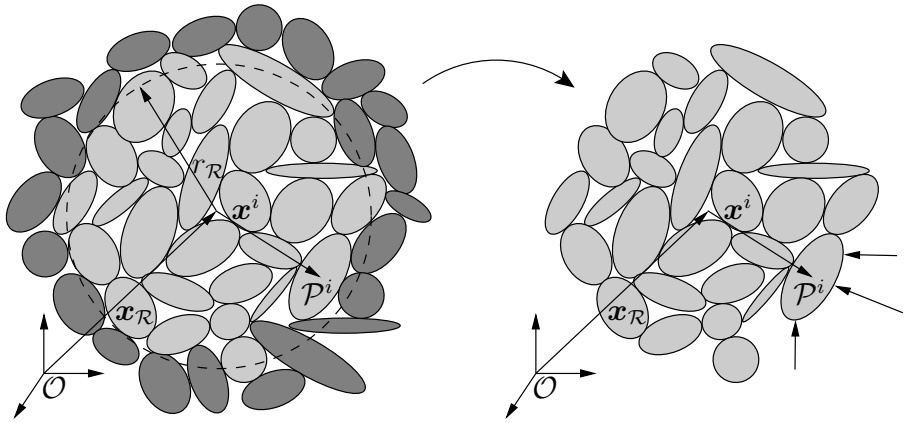


Fig. 6. Generation of an RVE $\mathcal{R}$. The lighter particles belong to $\mathcal{R}$. For the boundary particle $\mathcal{P}^i$ the outside contact forces are shown.

static deformation seems justified.

# 5 Homogenization

The results of a DEM simulation are given in terms of inter-particle contact forces and particle trajectories. To derive the macroscopic mechanical behavior from these microscopic quantities a homogenization procedure is applied, which is described in detail in [17]. For convenience, its important features are summed up in the following. Starting point of the homogenization procedure is the introduction of representative volume elements (RVEs). An RVE consists of a number of adjacent particles and serves as averaging volume for the macroscopic quantities of interest. To be representative the size of an RVE has to be much greater than the size of a single particle, so that the RVE contains a huge number of particles. Under this condition a scale separation argument can be applied which yields a simplified expression for the RVE average of the stress tensor. The resulting expression is transformed into a boundary integral which in the discretized form yields the expression for the RVE average stress tensor

$$\langle \boldsymbol{\sigma} \rangle = \frac{1}{V_{\mathcal{R}}} \sum_{i=1}^{N_{\partial \mathcal{R}}} \boldsymbol{f}^i \otimes \boldsymbol{x}^i. \tag{29}$$

Herein $V_{\mathcal{R}}$ is the volume of the RVE $\mathcal{R}$ and $N_{\partial \mathcal{R}}$ is the number of boundary particles of $\mathcal{R}$, which is the number of particles belonging to $\mathcal{R}$ that are in contact with particles outside $\mathcal{R}$. $\boldsymbol{f}^i$ is the the resultant of the outside contact forces of the boundary particle $\mathcal{P}^i$ and $\boldsymbol{x}^i$ is the position of $\mathcal{P}^i$, compare Fig. 6. Note, that the RVEs are generated by setting a reference point $\boldsymbol{x}_{\mathcal{R}}$ and a radius $r_{\mathcal{R}}$ and selecting all particles whose center distance to $\boldsymbol{x}_{\mathcal{R}}$ is smaller than $r_{\mathcal{R}}$. This yields approximately spherical shaped RVEs what is advantageous for the evaluation of the macroscopic quantities.

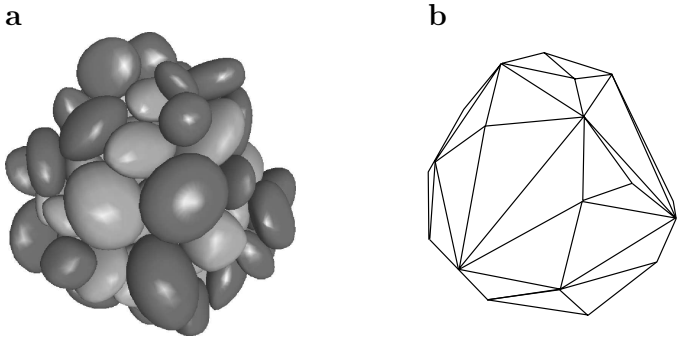


Fig. 7. RVE consisting of 76 particles. The centers of the darker particles in (a) specify the convex hull. (b) shows the corresponding triangular surface mesh.

An expression for the RVE average strain tensor is derived in a similar way. Here small displacements are assumed and the linear strain tensor is used. The volume average of the strain tensor is again transformed into a boundary term. The main difference between the derivation of average stresses and strains is that a discretized form of the RVE average stresses results naturally from the DEM results in terms of the contact forces while in the strain case the discretization of the RVE boundary has to be determined explicitly. Hence, a convenient definition of the RVE boundary for the strain case is required. Here the convex hull of all particle centers within an RVE is used which defines a unique boundary. This boundary is discretized in form of a triangular surface mesh whose vertices are the particle centers, see Fig. 7. This yields the discretized form of the RVE average strain tensor

$$\langle \boldsymbol{\epsilon} \rangle = \frac{1}{2\,V_{\mathcal{R}}} \sum_{ijk \in \mathbb{I}_{\mathcal{T}}} \left( \boldsymbol{u}^{ijk} \otimes \boldsymbol{n}^{ijk} + \boldsymbol{n}^{ijk} \otimes \boldsymbol{u}^{ijk} \right) A^{ijk} \,. \tag{30}$$

Herein $\mathbb{I}_{\mathcal{T}}$ is the set of index triples of the triangles belonging to the discretization and $\boldsymbol{u}^{ijk}$ is the average displacement, $\boldsymbol{n}^{ijk}$ the outward unit normal and $A^{ijk}$ the area of a triangle.
In order to get statistically meaningful results a number of RVEs has to be used to measure the macroscopic quantities so that ensemble averages and corresponding error bars can be computed. Since the average of a quantity $X$ over an RVE is denoted by $\langle X \rangle$ the average of $\langle X \rangle$ over all RVEs is denoted by $\langle\langle X \rangle\rangle$. The error bars are computed as

$$\left[ \langle\langle X \rangle\rangle - \frac{s\left(\langle X \rangle\right)}{\sqrt{N_{\mathcal{R}}}}, \langle\langle X \rangle\rangle + \frac{s\left(\langle X \rangle\right)}{\sqrt{N_{\mathcal{R}}}} \right] , \tag{31}$$

in which $s\left(\langle X \rangle\right)$ is the standard deviation and $N_{\mathcal{R}}$ is the number of RVEs. For the evaluation of the results from the numerical tests described in section 4 eight RVEs are generated using the same radius $r_{\mathcal{R}}$. Four different values for $r_{\mathcal{R}}$ were tested to analyze the influence of the RVE size on the fluctuation between the RVEs. The following table lists the radius $r_{\mathcal{R}}$ that was used to generate the RVEs and the corresponding average number of particles $\bar{N}_{\mathcal{P}}$ that belong to an RVE.

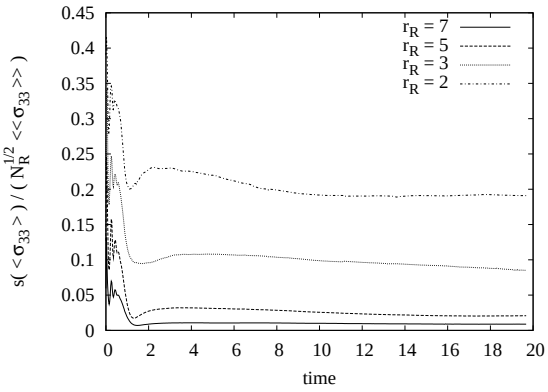


Fig. 8. Fluctuations of compression test results for different RVE sizes. The ratio of the error bar size and the mean value of the normal stress in loading direction is plotted against the simulation time.

| $r_{\mathcal{R}}$ | 2.0 | 3.0 | 5.0 | 7.0 |
|---|---|---|---|---|
| $\bar{N}_{\mathcal{P}}$ | 5.25 | 18.25 | 83.50 | 227.38 |

Fig. 8 compares the fluctuations for the different RVE sizes for a compression test. Here the ratio of the error bar size and the mean value of the normal stress in the loading direction is plotted against the simulation time for the different RVE sizes. It can be seen that after some oscillations in the beginning of the simulation all curves stay approximately at a constant value which decreases with increasing RVE size. The error bar size is about 20% of the mean value for $r_{\mathcal{R}} = 2$, 8% for $r_{\mathcal{R}} = 3$, 2% for $r_{\mathcal{R}} = 5$ and 1% for $r_{\mathcal{R}} = 7$. Considering the big difference between the results for $r_{\mathcal{R}} = 2$ and $r_{\mathcal{R}} = 3$ on the one hand and the relative close results for $r_{\mathcal{R}} = 5$ and $r_{\mathcal{R}} = 7$ on the other hand an RVE size of $r_{\mathcal{R}} = 5$ was chosen for the analyses of the compression and shear test results in section 6.

# 6 Results

As mentioned in section 4 the mechanical response of the particle sample depends on three microscopic constitutive parameters for both contact formulations. If, for the qualitative comparison of the results, the stresses are normalized there are only two influencing parameters left. For the penalty case this might be seen by looking at the constitutive equations (5) and (7) which state that the elastic contact force is proportional to the penalty parameters $c^N$ and $c^T$. Consequently, from equation (29), the stresses are proportional to the penalty parameters. Therefore the normalized stresses only depend upon the coefficient of friction $\mu$ and the ratio of the penalty parameters $c^T/c^N$. This was checked by repeating a compression test with different values of $c^N$ while keeping $c^T/c^N$ constant. In the same way the only parameters influencing the normalized stresses when using the HERTZIAN type contact model are the coefficient of friction $\mu$

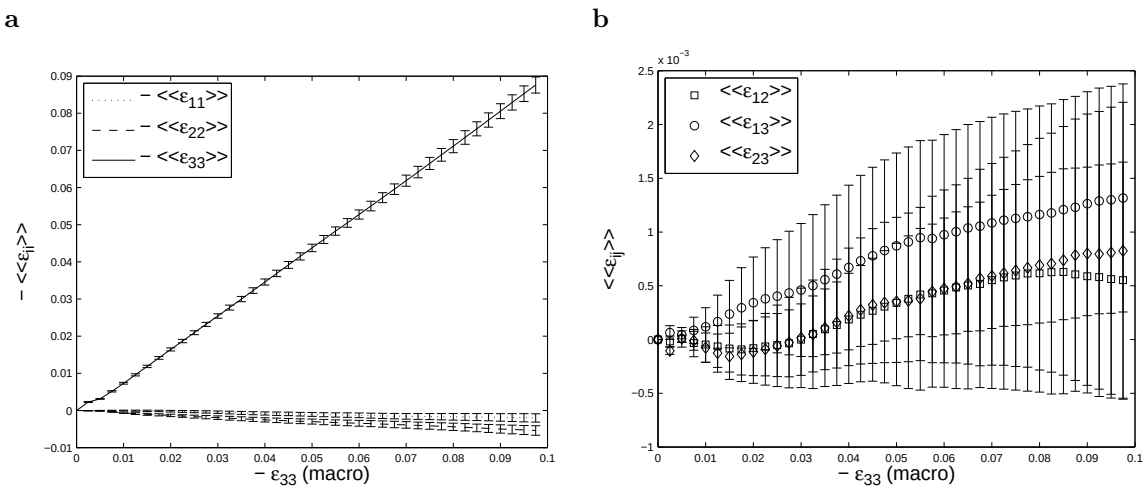


Fig. 9. Normal (a) and shear (b) strains vs. macroscopic compression strain for a compression test using the HERTZIAN contact formulation with $\mu = 0.5$ and $\nu = 0.22$ .

and POISSON's ratio $\nu$. This is because the elastic contact force is proportional to the elastic modulus as follows from equation (12), (13) and (19) to (24).

First, the compression test results will be described. Fig. 9 shows the RVE average strains for a test with an end compression of $c_{\text{end}} = 0.1$ using the HERTZIAN contact formulation with $\mu = 0.5$ and $\nu = 0.22$. As expected, the results of tests with different parameters and tests using the penalty type contact formulation pointed out that the strain results are independent of both the contact formulation and the parameters chosen. As can be seen in Fig. 9 there is a good agreement of the RVE average strains and the macroscopic alleged strains from equation (27). The normal stress in the loading direction rises linear with its corresponding macroscopic value and they differ by about 10%.

Fig. 10 shows plots of the normalized negative normal stresses $-\langle\langle\sigma_{ii}\rangle\rangle/\max(|\langle\langle\sigma_{33}\rangle\rangle|)$ over the compression strain $-\langle\langle\epsilon_{33}\rangle\rangle$ using the penalty contact formulation with $c^T/c^N = 1.0$ and $\mu = 0.5$ (a) and the HERTZIAN contact formulation with $\nu = 0.22$ and $\mu = 0.5$ (b). While there is a linear rise of the normal stresses with the compression strain in the penalty case the stresses behave nonlinear for the HERTZIAN contact formulation with the stiffness increasing with increasing compression. The ratio of the stress in the loading direction and the stresses perpendicular to the loading direction is similar for both contact formulations.

To analyze the influence of the microscopic constitutive parameters the compression test was repeated with a number of different parameter combinations. To reduce the computational effort the end compression was set to $c_{\text{end}} = 0.4$ for these tests. For the discussion of the results the deviator stress $q$ and the mean principal stress $p$ are introduced, which are commonly used to describe the results of triaxial tests of granular material. They are defined in terms of the

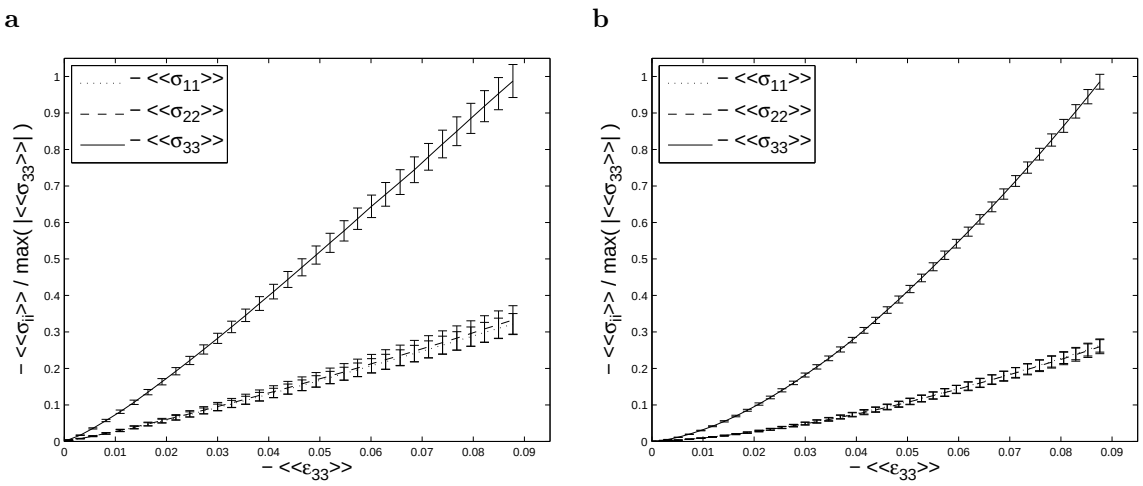


Fig. 10. Normalized negative normal stresses for compression tests using the penalty contact formulation with $c^T/c^N = 1.0$ and $\mu = 0.5$ (a) and the HERTZIAN contact formulation with $\nu = 0.22$ and $\mu = 0.5$ (b) .

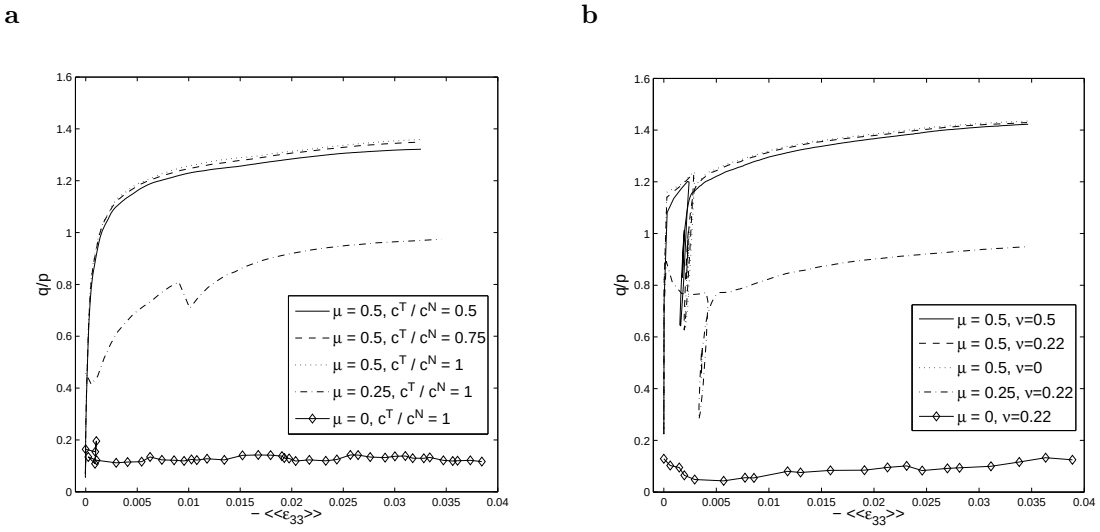


Fig. 11. Ratio of the deviator stress $q$ and the mean principal stress $p$ for the penalty (a) and the HERTZIAN (b) contact formulation .

principal stresses through

$$q = \sigma_1 - \sigma_3 \,, \tag{32}$$

$$p = (1/3)\,(\sigma_1 + \sigma_2 + \sigma_3) \,. \tag{33}$$

For the compression test the principal stresses are $\sigma_1 = \langle\langle\sigma_{33}\rangle\rangle$ and $\sigma_2 = \sigma_3 = \langle\langle\sigma_{11}\rangle\rangle = \langle\langle\sigma_{22}\rangle\rangle$. Note, that in equation (32) the equality of $\sigma_2$ and $\sigma_3$ has been used to simplify the expression for $q$. In Fig. 11 the stress ratio $q/p$ is plotted against the compression strain for both contact formulations and the different parameter combinations. For the tests without inter-particle friction ($\mu = 0$) the stress ratio has an approximately constant value of about 0.1 for both contact

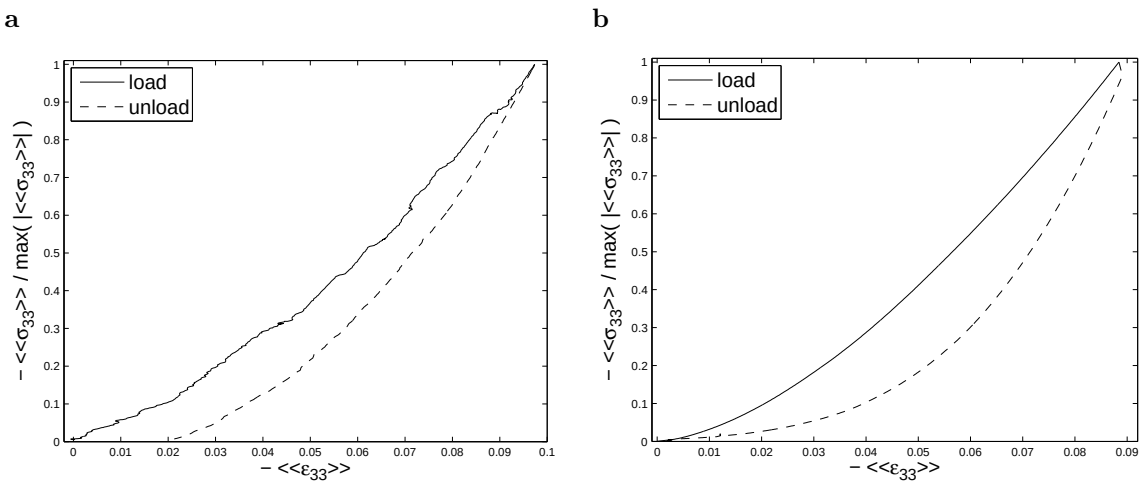


Fig. 12. Comparison of the loading and unloading stress-strain paths of the compression test using the HERTZIAN contact formulation with $\nu = 0.22$, $\mu = 0$ (a) and $\mu = 0.5$ (b) .

formulations which corresponds to a nearly hydrostatic stress state. The other curves increase with decreasing slopes and tend towards constant values what is typical for triaxial compression tests of granular media. The sharp peaks for the HERTZIAN contact formulation at compression strains of about 2% and 4% respectively are believed to be due to sudden particle slippage resulting in dynamic effects which influence the stresses for a short period of time. Regarding the microscopic parameters it can be seen that the influence of the ratio of the penalty parameters $c^T/c^N$ and POISSON's ratio $\nu$ respectively is negligible when compared with the influence of the coefficient of friction $\mu$. A decrease of $\mu$ results in a decrease of the stress ratio which corresponds to a loss of the materials ability to withstand shear stresses. The reason for the small influence of $c^T/c^N$ and $\nu$ on the stress ratio is that the deformation of the particle sample is mainly due to slippage of the particles. Hence, the upper bound for the tangential contact force defined by the coefficient of friction and the normal contact force is reached at most of the contacts. In this case the ratio of the tangential and normal stiffness of a contact which depends upon $c^T/c^N$ and $\nu$ respectively no longer has an influence on the contact force.

To support the argument of particle slippage the unloading paths of two compression tests were analyzed. If remarkable particle slippage occurs during the deformation of the particle sample the loading and unloading path should show a hysteresis. Fig. 12 shows that this is the case for both of the tests. Here the normalized compression stress is plotted against the compression strain for the tests using the HERTZIAN type contact formulation with $\nu = 0.22$ and $\mu = 0$ or $\mu = 0.5$ respectively. For $\mu = 0$ it can be seen that the stiffness of the system when unloaded from the maximum compression is approximately the same as on the loading path. The unloading path then decreases with the same nonlinear behavior as the loading path and finally ends at a plastic

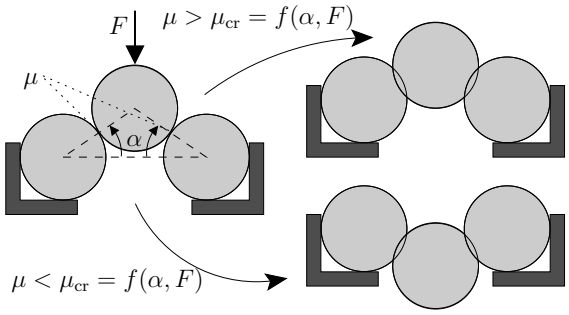


Fig. 13. Simple example to demonstrate the effect of particle slippage. For $\mu < \mu_{cr}$ the upper particle will slip through the others resulting in an irrecoverable deformation of the system.

compression strain of about 2%. For $\mu = 0.5$ there is a clear increase in stiffness from the loading to the unloading path at the maximum compression. The unloading path has a greater curvature than the loading path and ends at zero compression.

These behaviors are best understood by considering the simple example depicted in Fig. 13. The upper particle initially rest on the other particles with the lines connecting their centers inclined by an angle $\alpha$. A vertical load $F$ is applied to the upper particle pressing it against the other particles. Assuming that the normal contact forces alone are to small to prevent the upper particle from slipping through the others, there will be a critical coefficient of friction to prevent the particle from slipping through. This coefficient of friction $\mu_{cr}$ will be a function of the inclination angle $\alpha$ and the loading force $F$. For $\mu > \mu_{cr}$ the deformation of the system will be fully recovered when the load is removed while for $\mu < \mu_{cr}$ the deformation is irrecoverable. Fig. 14 shows a section of the particle sample before and after the compression for a test without inter-particle friction. In the region marked by the dashed ellipse the particles rearrange during the compression resulting in an irrecoverable deformation. Considering the stress-strain paths in Fig. 12 the difference between $\mu = 0$ and $\mu = 0.5$ can now be explained in the following way: For $\mu = 0$ a significant part of the deformation is irrecoverable resulting in the plastic strain while for $\mu = 0.5$ the irrecoverable part of the deformation is negligible. The change in stiffness from the loading to the unloading path at maximum compression for $\mu = 0.5$ results from particle slippage: If two contacting particles slip on the loading path, the tangential contact force acts plastically in the sense that there is no increase of the tangential force with relative displacement of the particles. If the system is unloaded the relative particle motion is expected to invert resulting in an immediate decrease of the tangential contact force. This difference between the plastic response on the loading path and the elastic response on the unloading path results in a remarkable change in the overall stiffness of the system if particle slippage occurs at a significant fraction of the contacts.

However, the irrecoverable deformation for $\mu = 0$ is expected to act in a similar way on the

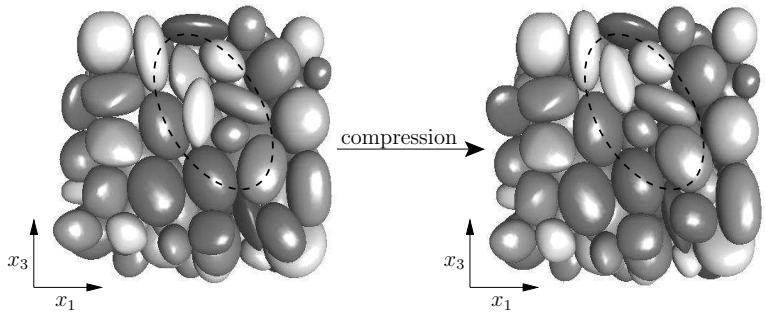


Fig. 14. Irrecoverable deformation due to particle rearrangement for a compression test without inter-particle friction.

overall stiffness but here a change in stiffness is not detected at the maximum compression level. This is believed to be mainly due to the following reasons: First, the greatest part of the irrecoverable deformation is expected to happen at lower compression levels because here more free space is available for particle rearrangements. Second, the slip-through events result in an increase of dynamic effects in the particle system which in turn results in the roughness of the loading path for $\mu = 0$. This roughness makes it hart to clearly identify the slope of the curve at maximum compression. Note, that the amount of plastic deformation shown by the particle sample is small compared to real granular materials. This is believed to be mainly due to the relatively small ratio of the particle size to the system size, which was chosen to keep the computation time in an acceptable range (a compression test with $c_{\text{end}} = 0.1$ took approximately one day of CPU time on a 3GHz machine).

The intermediate configurations of the compression test were then used as initial configurations for the shear test. Herein the initial compression in the $x_3$ direction was chosen as $c_{\text{end}} = 0.04$, compare equation (28). The final shear angle was set to $\gamma_{\text{end}} = 0.2$ resulting in a maximum macroscopic shear strain of $\epsilon_{13} = 0.1$. For the evaluation of the results the strain datum was set to the initial configuration of the shear test so that all strains in Fig. 15 start from zero. Here the RVE average volumetric strain (a) defined by

$$\epsilon_{\text{vol}} = (1/3)\ (\langle\langle\epsilon_{11}\rangle\rangle + \langle\langle\epsilon_{22}\rangle\rangle + \langle\langle\epsilon_{33}\rangle\rangle) \tag{34}$$

and the RVE average shear strains (b) are plotted against the macroscopic shear strain in the loading direction. Like for the compression test there is a good agreement of the macroscopic alleged and the RVE average strains. The shear strain in the loading direction $\langle\langle\epsilon_{13}\rangle\rangle$ increases linearly with its macroscopic counterpart and they differ in magnitude by less than 10% while the other shear strains are negligible. Looking at the volumetric strain one can see that the volume of the particle sample initially decreases until a shear strain of about 5%. From there on the sample dilates until the final shear strain. This is the typical behavior of dense granular samples in the

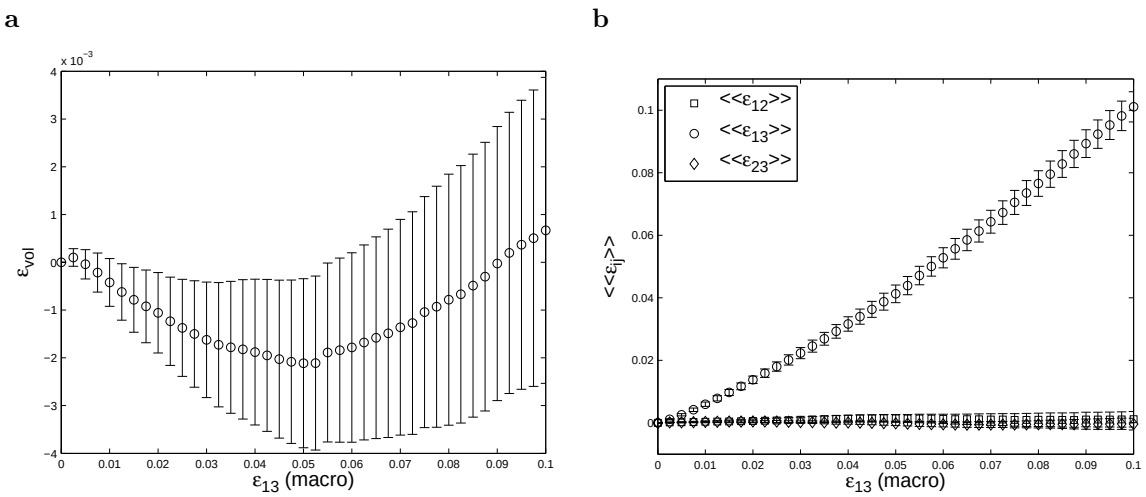


Fig. 15. Volumetric (a) and shear (b) strains vs. macroscopic alleged shear strain for a shear test using the HERTZIAN contact formulation with $\mu = 0.5$ and $\nu = 0.22$ .

shear-box test which is commonly used to determine the shear strength of soils, see e.g. [13]. Fig. 16 compares the RVE average stresses resulting from the penalty contact formulation with $c^T/c^N = 1$ and $\mu = 0.25$ and the HERTZIAN contact formulation with $\nu = 0.22$ and $\mu = 0.25$. Herein the stresses are normalized with the initial value of the volumetric stress

$$\sigma_{\text{vol}} = (1/3)\ (\langle\langle\sigma_{11}\rangle\rangle + \langle\langle\sigma_{22}\rangle\rangle + \langle\langle\sigma_{33}\rangle\rangle)\ . \tag{35}$$

All curves show the same characteristics for both contact formulations. The normal stresses increase with the shearing strain where $\langle\langle\sigma_{33}\rangle\rangle$ initially decreases until a shearing strain of about 5% for the penalty and 2% for the HERTZIAN contact formulation. After this the curves of all components have similar slopes. The shear stress in loading direction shows a nonlinear behavior with the stiffness decreasing until a shear strain of about 4% and remaining constant from there on. The other shear stresses are negligible. The major differences between the contact formulations are that the increase of the normal stresses is greater for the HERTZIAN contact formulation and that the shear stress reaches a higher value compared to the initial volumetric stress for the HERTZIAN contact formulation. Here it has to be noted that the stresses resulting from the different contact formulations are normalized with different initial volumetric stresses. Therefore, the results in Fig. 16 might be influenced by the absolute value of the penalty parameters $c^N$ and $c^T$ and the value of the elastic modulus $E$ respectively. The choice of a higher $E$ e.g. will yield a higher volumetric stress for the same initial compression of the shear test sample. This higher initial volumetric stress in turn will facilitate higher shear stresses but the relation between the rise in the initial volumetric stress and the rise in the resulting shear stress might not be linear so that the run of the curves in Fig. 16 will be influenced. Hence, the main result of this comparison is that both contact formulations show the same characteristics for all

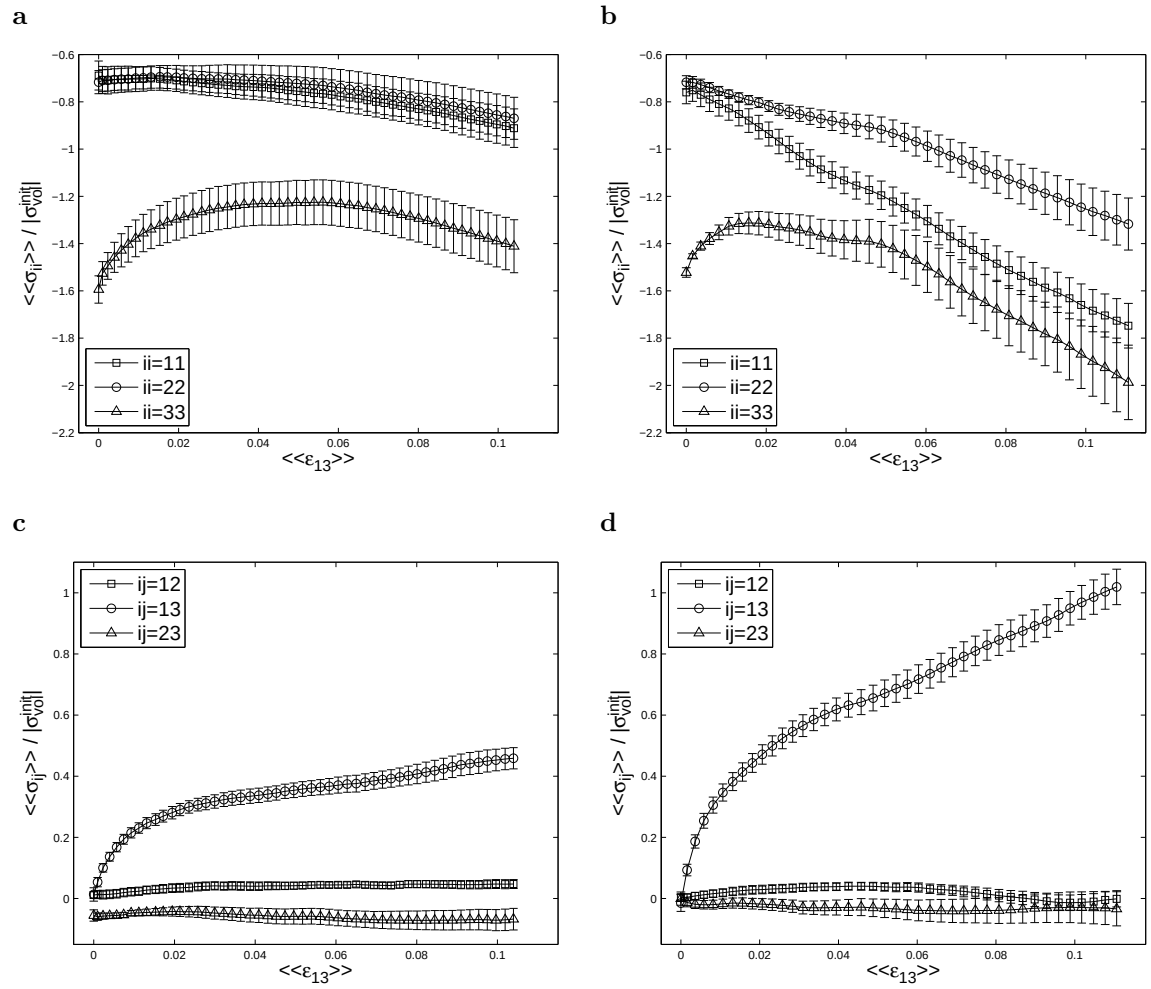


Fig. 16. Normalized stresses for shear tests with $\mu = 0.25$. (a),(c): Normal and shear stresses using the penalty contact formulation with $c^T/c^N = 1$. (b),(d): Normal and shear stresses using the HERTZIAN contact formulation with $\nu = 0.22$.

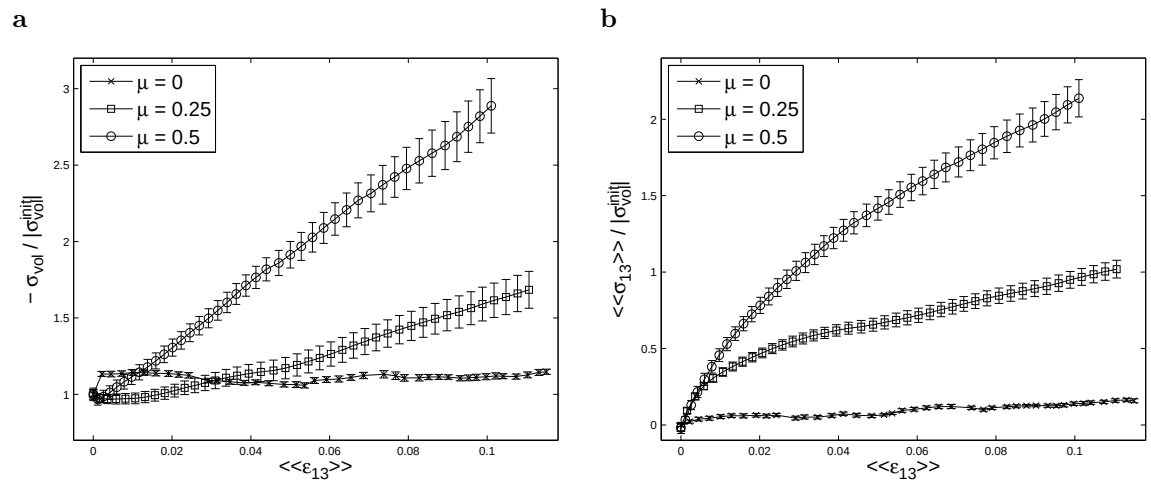


Fig. 17. Normalized volumetric (a) and shear stress (b) using the HERTZIAN contact formulation with $\nu = 0.22$ and varying coefficient of friction $\mu$.

stress components.

To analyze the influence of the coefficient of friction the shear test was repeated using the HERTZIAN contact formulation with $\mu = 0$ and $\mu = 0.5$. The results are shown in terms of the volumetric stress $\sigma_{\text{vol}}$ and the shear stress $\langle\langle\sigma_{13}\rangle\rangle$ in Fig. 17. It can be seen that without inter-particle friction the stresses remain approximately constant during the shear deformation. Hence, the particle system stays in the hydrostatic state like in the compression test. Comparing the plots for $\mu = 0.25$ and $\mu = 0.5$ it becomes apparent that an increase in the coefficient of friction leads to higher volumetric as well as higher shear stresses. While for $\mu = 0.5$ the final volumetric stress is about three times the initial volumetric stress the ratio is only about 1.7 for $\mu = 0.25$. The plot of the shear stresses shows that the initial shear stiffness of the system is approximately the same for $\mu = 0.25$ and $\mu = 0.5$. The stiffness than decreases until a shear strain of about 4% and remains approximately constant from there on. This constant stiffness is greater for $\mu = 0.5$ resulting in a final value of the shear stress for $\mu = 0.5$ of about twice the initial volumetric stress while the final ratio for $\mu = 0.25$ is about one.

# 7 Conclusion

Within this paper two microscopic constitutive formulations for inter-particle contacts were compared in terms of the macroscopic mechanical behavior arising from them. The description of this behavior was gained in two steps: First, three-dimensional DEM simulations of a cuboid particle sample were performed. Second, a homogenization procedure was applied to transfer the inter-particle contact forces and particle trajectories resulting from a DEM simulation into stresses and strains. Compression and shear tests were performed for both contact formulations

and various sets of the corresponding microscopic constitutive parameters.

One of the main results of the comparison is that the HERTZIAN contact formulation yields more realistic results for the compression test when compared to results of standard odeometer tests of real granular materials. Here the HERTZIAN contact formulation yields a nonlinear behavior with increasing stiffness of the particle sample while the stiffness remains constant when the penalty contact formulation is used. Regarding the shear strength of the particle sample and its related characteristics it was found that the different contact formulations yield qualitatively very similar results. Further it could be shown that the shear behavior of the particle sample depends more or less solely on the choice of the microscopic coefficient of friction.

An important advantage of the HERTZIAN contact model lies in the nature of the microscopic constitutive parameters that are used. While the penalty contact formulation uses penalty parameters which lack of a real physical meaning, the HERTZIAN contact formulation uses the elastic constants of the particles, which might be determined experimentally for the simulation of real granular materials. The major drawback of the HERTZIAN contact formulation is the increase in computational costs when compared to the penalty contact formulation which results from the need of a refined description of the contact geometry including the principal curvatures and the approximation of elliptic integrals. This increase can be reduced significantly if it is possible to reuse the geometry parameters of a contact pair for a number of time-steps. For example, the final compression for the compression tests shown here was applied in 200000 DEM time-steps. Most of the particle contacts remain for a huge number of time-steps and the geometry parameters change only very little between subsequent time-steps. A less important problem of the HERTZIAN contact formulation is that the contact stiffnesses vary throughout the particle system and with time. This is a problem because the critical time-step size that might be used for the DEM simulation depends primarily on the contact stiffnesses and the particle masses, compare [12] (the DEM simulations whose results were shown here were run with a constant time-step size, which was checked by monitoring the energy of the particle system).

Interesting future problems will be the analyses of the influence of a) the particle shape and b) the particle size distribution on the macroscopic behavior of an assemblage of particles. For this purpose a convenient scheme to generate random particle packages will be required, which is computationally cheaper than the scheme described in section 4. Furthermore the DEM simulation itself might be speed up through parallelization to facilitate analyses of greater particle systems within an acceptable amount of CPU time.

# References

[1] M. Abramovitz and I. Stegun. *Handbook of Mathematical Functions With Formulas, Graphs, and Mathematical Tables*. Dover Publications, 1972.

[2] J-F. Antoine, C. Visa, C. Sauvey, and G. Abba. Approximate analytical model for hertzian elliptical contact problems. *Journal of Tribology*, 128(3):660–664, 2006.

[3] A. H. Barr. Superquadrics and angle-preserving transformations. *IEEE Computer Graphics and Applications*, 1(1):11–23, 1981.

[4] P. A. Cundall. A discontinuous future for numerical modelling in geomechanics? *Geotechnical Engineering*, 149(1):41–47, 2001.

[5] P. A. Cundall. Formulation of a three-dimensional distinct element model. i: A scheme to detect and represent contacts in a system composed of many polyhedral blocks. *International Journal of Rock Mechanics and Mining Sciences*, 25(3):107–116, 1988.

[6] P. A. Cundall and O. D. L. Strack. A discrete numerical model for granular assemblies. *Geotechnique*, 29: 47–65, 1979.

[7] G. M. L. Gladwell. *Contact problems in the classical theory of elasticity*. Sijthoff & Noordhoff, Alphen aan den Rijn, The Netherlands, 1980.

[8] H. Hertz. Über die berührung fester elastischer körper (on the contact of elastic solids). *Journal für die reine und angewandte Mathematik*, 92:156–171, 1882.

[9] K. L. Johnson. *Contact Mechanics*. Cambridge University Press, 1985.

[10] X. Lin and T.-T. Ng. A three-dimensional discrete element model using arrays of ellipsoids. *Geotechnique*, 47 (2):319–329, 1997.

[11] R. D. Mindlin. Compliance of elastic bodies in contact. *Journal of Applied Mechanics*, 16:259–268, 1949.

[12] C. O'Sullivan and J. D. Bray. Selecting a suitable time step for discrete element simulations that use the central difference time integration scheme. *Engineering Computations*, 21(2/3/4):278–303, 2004.

[13] W. Powrie. *Soil Mechanics*. Spon Press, 2004.

[14] E. Rougier, A. Munjiza, and J. P. Latham. Shape selection menu for grand scale discontinua systems. *Engineering Computations*, 21(2/3/4):343–359, 2004.

[15] A. M. Sallam. *Studies on Modeling Angular Soil Particles Using the Discrete Element Method*. PhD thesis, University of South Florida, College of Engineering, 2004.

[16] C.-Y. Wang, C.-F. Wang, and J. Sheng. A packing generation scheme for the granular assemblies with 3d ellipsoidal particles. *International Journal for Numerical and Analytical Methods in Geomechanics*, 23(8): 815–828, 1999.

[17] C. Wellmann, C. Lillie, and P. Wriggers. Homogenization of granular material modeled by a three-dimensional discrete element method. Accepted for publication in Computers and Geotechnics.

[18] J. R. Williams and A. P. Pentland. Superquadrics and modal dynamics for discrete elements in interactive design. *Engineering Computations*, 9(2):115–127, 1992.